Generation of High-Order Waveguide Modes with Reduced Symmetric Protection

High-Order Waveguide Mode Generations with Reduced Symmetric Protection

Jianfeng Chen[1], Qiang Cheng[1,†], Wei Yuan[1], Li Wang[1], Wen Xuan Tang[1], Lei Wang[2], and Tie Jun Cui[1,*]

[1] *State Key Laboratory of Millimeter Waves, Department of Radio Engineering, Southeast University, Nanjing 210096, People's Republic of China*

[2] *School of Engineering and Physical Sciences, Heriot-Watt University, Edinburgh EH14 4AS, U.K*

[†]Jianfeng Chen and Qiang Cheng contributed equally to this work

[†]qiangcheng@seu.edu.cn

[*]tjcui@seu.edu.cn

Single-mode operation in a rectangular waveguide is very important, since the existence of multi-modes may arouse distortions of carried signals due to the modal dispersion. High-order mode means multiple periods of field in the transverse cross section, with distinct electromagnetic properties from the dominant mode. Although numerous methods have been proposed to achieve mode selection within the waveguide, they only permit specific high-order modes to survive in a frequency range. However, it still remains a great challenge to control the bandwidth freely for single mode operation. Here, we propose an approach for high-order mode generation, in which the desired mode operates in the bandgap of other modes, and the working bandwidth can be engineered independently by reducing the symmetry of the loaded periodic metallic ridges in the waveguide. Two examples are demonstrated where only TE_{20} and TE_{30} modes are supported, respectively. The proposed method can also be applied to generate other high-order TE modes in the future.

I. INTRODUCTION

Waveguides as an important family of transmission line to route the electromagnetic waves and convey the energy between two endpoints, have been widely employed to realize a bunch of microwave or optical components including the filters, couplers, isolators, resonators, antennas and power dividers, showing the advantages of low transmission loss, broad bandwidth and high power-handling capability. Initially, the single mode operation is highly required to achieve high transmission efficiency and stable system performance, where tremendous efforts had been made to suppress high order modes and improve the single mode bandwidth [1-6]. However, with the rapid advance of the waveguide technology, the high order modes have gained more and more interest and witnessed successful applications such as power combining, high-power electron devices, microwave heating and millimeter wave antennas [7-19].

In general, when we deal with the high order modes in traditional waveguides, the fundamental mode usually exists in the meanwhile, making it hard to extract the desired order mode for device and antenna design. To overcome this limitation, several approaches have been proposed to realize the high order mode generation. One way is to introduce discontinuities inside the waveguide. For instance, a right-angled corner was used to connect two different sized waveguides so as to realize the conversion from TE_{10} to TE_{20} mode. Several metallic posts were placed in this corner to suppress the dominant TE_{10} mode [20-23]. Another option to reach that goal is shifting the feeding point some distance from the center, which can enhance the intensity of TE_{20} mode and suppress the generation of TE_{10} mode in the meanwhile [24].

Here, we report on an alternative method to generate a single high order mode in a rectangular metallic waveguide with the symmetric protection technology. To eliminate the fundamental TE_{10} of the rectangular waveguide, periodic metallic ridges are loaded at the top and bottom waveguide surfaces to form a bandgap for the TE_{10} mode within the spectrum of interest, where only the desired TE_{20} mode can survive. The reduced glide symmetry of the ridges is introduced to adjust the symmetric protection in the proposed waveguide, since the degree of glide symmetry breaking is to determine the range of the bandgap for the fundamental mode with the bandgap center unchanged. Thereby it allows us an unprecedented

control over the propagation characteristics of the single high order mode such as the working bandwidth and central operation frequency. Similarly, the generations of single TE_{30} mode is also implemented in theory and experiment as well, by controlling the dimensions of the periodically-loaded ridges. In contrast to the reported high order mode converting strategies in the past decades [22-24], our scheme stands out as for its simple structure, easy implementation, customized bandwidth and high mode purity, which provides exceptional flexibility for mode manipulation in the engineering. To confirm the validity of our findings, both the numerical and experimental studies have been carried out to investigate the mode properties of a ridge-loaded rectangular waveguide. By engineering the reduced glide symmetry of the ridges, we verify the feasibility of the single high order mode generation in the microwave region. Due to the advantages of high-order TE_{n0} mode purity and easy design of the proposed structure, we believe that this investigation gives inspiration for the application of 1-to-*n* power dividers and phase shifters, especially in the millimeter wave band, since the electric separations between the adjacent channels can be removed, which is helpful for simplifying the geometry.

II. THEORY AND DESIGN

The electromagnetic (EM) field distributions within a waveguide can be obtained by solving the wave equations with the corresponding boundary conditions. In general, a knowledge of the longitudinal components for both electric and magnetic fields is sufficient to determine the total fields inside the waveguide [25]. For a guided wave structure with regular cross section, there exist a number of discrete solutions in regard to the wave equations, corresponding to various waveguide modes in reality. Each mode is associated with a cutoff frequency, beyond which the mode can propagate with little attenuation within the waveguide. Take the rectangular waveguide in Fig. 1(a) for example, the coexistence of the first and second order modes can be clearly observed at high frequencies from the gray region of the modal dispersion diagram in Fig. 1(b). In fact, the first order mode can never be efficiently removed due to the lowest cutoff frequency, implying that the high order mode is hard to exist inside the waveguide on its own.

To circumvent this problem and change the mode dispersions, we need to modify the

boundary conditions of the waveguide, giving rise to the desired mathematical representations of the solutions to wave equations. Here we consider the rectangular waveguide loaded by periodic structures, which is widely applied in microwave engineering to realize functionalities such as microwave filters, traveling-wave antennas, and microwave tubes. For a periodic structure in Fig. 1(c), it supports a set of Bloch modes that are closely related to the structural symmetry according to the Floquet's theorem [26-28]. Under this circumstance, the waveguide loaded with periodic structures behaves as a one-dimensional photonic crystal, which is featured by the emergence of the bandgap in which the original waveguide mode is no longer supported due to the multiple scattering between the unit cells. As illustrated in Fig. 1(d), the dispersion curve of the original fundamental mode (TE_{10} mode) is split into a set of spatial harmonics [30], with the formation of bandgaps at the split point where $\beta L = n\pi$ (L is the loading period, n is an integer) [30]. Additionally, the high order modes are often found to exist out of the bandgap. As a result, it makes the periodically loaded waveguide a good candidate for the band rejection filter in the engineering, which is extensively investigated in a lot of literature in the past two decades [32-33].

However, a question then naturally arises whether the specific high order waveguide mode can fall into the bandgap of the fundamental mode as shown in Fig. 1(e), since it would offer an efficient avenue to realize single high order mode operation that is extremely desired in many situations. Actually, as revealed by the numerical simulations later, this goal can be achieved by carefully optimizing the element shapes and dimensions, and we successfully demonstrate the feasibility to allocate the desired high order mode into the apparently forbidden region. This really makes sense because, for infinitely periodic structure, the upper and lower edge frequencies of the bandgap can be calculated using Bragg diffraction condition, as:

$$2k \cdot G = G^2, \tag{1}$$

where $\boldsymbol{k}$ is the wave vector (correspond to $\boldsymbol{\beta}$ in 1-D period system), $\boldsymbol{G}$ is the reciprocal vector of the period lattice. Note that, the wave vector for each mode is distinct, showing that the diversity of Bragg diffraction condition for different modes. Therefore, each stopband only works for its corresponding mode.

Next, we proceed to investigate the feasibility of the bandwidth control for single high order mode operation. It is well known that the bandgap of the fundamental mode can be adjusted by altering the geometry of the unit cell as well as the periodicity. However, the change of the structural dimensions usually leads to the offset of the bandgap center [20-24] despite the bandgap width can be effectively modified, therefore greatly limits in their applicability to reconfigurable devices.

Indeed, an additional degree of freedom can be introduced to customize the bandgap bandwidth while keeping stable central frequency, which explores the variation of the element symmetry along the propagation direction of the guided waves. Specifically, a periodically loaded structure is said to possess glide symmetry if it is coincident with itself under the glide operation G as follows [30-31]:

$$G=\begin{cases} x \to -x \\ y \to y \\ z \to z+L/2 \end{cases}, \tag{2}$$

and the wavenumbers of the periodic structure with normal and glide symmetry (β_T and β_G) are connected by:

$$\beta_T L=\beta_G L+2\pi v, \quad v=0, 1. \tag{3}$$

where L is the periodicity and v is a natural number [30]. When the glide symmetry is applied for the periodic structures, the bandgap between the two branches of the dispersion curves can be eliminated from the coupled mode theory [29-30]. For a periodic structure with normal symmetry, the coupling between two harmonic modes can happen at the points $\beta L=n\pi$. The power flow of one harmonic mode will be completely offset by the other. As a result, the net power flow equals to zero based on the conservation of energy. The degeneracy point will split up, assuming that there is no source of energy in the guiding structure. However, the harmonic branches are uncoupled at $\beta L=\pi$ for the case of glide symmetry. So, these uncoupled modes corresponding to different branches of the dispersion curves, are able to cross (degeneracy) when v is odd [29]. According to the difference of the dispersion characteristics for periodic structure with normal and glide symmetry, it is rational to adjust the bandwidth by breaking glide symmetry of the elements, resulting in the disappearance of the degeneracy point and the formation of the expected stopbands. During the transition from glide symmetry to normal

symmetry, the bandgap width is gradually increased with fixed central frequency, which suggests that the symmetry control offers an important tool to manipulate the bandgap of the fundamental mode for high order mode operation.

To validate the proposed theory, a periodically ridge-loaded rectangular waveguide is designed to realize high order mode operation. In the microwave engineering, the metallic ridge is widely employed to reduce the cutoff frequency of the fundamental mode, and thereby minimize the dimensions of the cross section and achieve good impedance matching. However, here we try to adjust the symmetry of the loaded metallic ridges to change the bandgap behavior as depicted in Fig. 2(a). We consider the waveguide with the lateral dimensions of 16 *mm* and 10 *mm*. The ridge length, width and period are a, b and L respectively. The ridges are arranged alternatively on the top and bottom plates as marked by red and green in Fig. 2(a), with the separation distance of L_1. The full wave simulation package CST 2018 is performed to observe the modal distributions inside the waveguide. Initially when the glide symmetry of the loaded ridges is assumed with $L_1 = L/2$, and only one ridge is placed in the lateral direction, the TE_{10} mode is generated as predicted by the classical electromagnetic theory as shown in Fig. 2(a). Interestingly, if the width of the waveguide is doubled transversely with two ridges aligned side by side (see right, the bottom panel of Fig. 2(a)), the dominant mode changes into TE_{20} mode as depicted by the field distributions in the waveguide cross section in Fig. 2(b). By further increasing the waveguide width to allow more ridges in the transverse direction, we clearly see the excitation of the high order TE_{30}, TE_{40} modes, revealing that the waveguide width is a critical issue to be considered for high order mode generation.

In addition, the dispersion properties of the TE_{10} and TE_{20} modes are also studied with the dependence of the structural symmetry as displayed in Fig. 2(d). With the decrease of the spatial shift L_1 from $L/2$ to 0, the glide symmetry is broken and the normal symmetry is finally achieved when L_1 reaches zero. The electromagnetic bandgap starts to arise for TE_{10} mode and then becomes larger and larger as the shift L_1 shrinks. On the contrary, only TE_{20} mode can be supported within the gap, which offers the possibility of single mode operation as desired. It is worth noting that the central frequency is hardly affected by the change of the bandgap, which provides great convenience to adjust the bandwidth of the single high order mode operation.

One important aspect that needs to be further explored is the excitation of the single high order mode within the waveguide. Although the high order mode can be produced by increasing the waveguide width, we notice that TE_{n0}^{nw} and TE_{10}^{w} actually have identical dispersion features in the Brillouin zones, where *n* is the mode index, and the superscript represents the corresponding waveguide width for better understanding. As is well known, the propagation constant of TE_{n0} mode can be expressed as $\beta^2 = k_0^2 - (n\pi / w_g)^2$, in which k_0 and w_g are the freespace wavenumber and the waveguide width respectively. Therefore when $w_g = nw$, we have the same propagation constant β for the modes TE_{n0}^{nw} and TE_{10}^{w} within the waveguides of different widths. Fig. 2(c) depicts the electric field distribution in the transverse cross section (*xoz* plane) for TE_{10}^{w}, TE_{20}^{w} and TE_{30}^{w} modes.

Due to the match of the propagation constants for the two modes, it enables us to construct a transition between two waveguides with various cross sections by directly connecting them together, without worrying much about the severe reflections at the waveguide junction. For instance, as illustrated in Fig. 3(a), the TE_{10}^{w} and TE_{20}^{2w} modes are generated in the left and right waveguides with the width ratio of 1:2, where the glide symmetric ridges are incorporated for the manipulation of mode dispersion characteristics. Here, the ideal waveguide ports are adopted to excite the desired waveguide modes. Because of the impedance and propagation constant differences between the empty waveguide and periodically loaded waveguide, tapered transitions are employed in our design [see the dotted rectangles in Figure 3(a)], which can help increase the conversion rate between various waveguide modes and remove unwanted wave reflections. The heights of the ridges are gradually increased from $h_r/3$ to h_r near Port 1 and Port 2. The simulated electric field distributions are reported in Fig. 3(b), and the perfect conversion can be observed from TE_{10}^{w} to TE_{20}^{2w} modes when passing through the transition.

The mode purity, as an important factor to evaluate the degree of single mode operation within the waveguide, is analyzed by the simulated transmission coefficients from TE_{10}^{w} to TE_{10}^{2w} and TE_{20}^{2w} modes respectively. Under the excitation of TE_{10}^{w} mode on the left side in Fig. 3(a), the magnitude ratio of output TE_{20}^{2w} ¿ TE_{10}^{2w} modes can be over 25 dB from 10.2 to 12 GHz (see Fig. 3(c)) when L_1/L equals to zero, implying that the incident mode is significantly suppressed in this case, and only the TE_{20}^{2w} *mode* is supported as the carrier wave for single mode operation. Note that the suffix of S_{21} in Fig. 3(c) represents the conversion rate from the latter to the former mode. For example, $S_{21}[TE_{20}^{2w} - TE_{10}^{w}]$ stands for the magnitude ratio between the output TE_{20}^{2w} mode to the input TE_{10}^{w} mode. The phenomenon is consistent with the theoretical discussions in Fig. 2(d), since the TE_{10}^{w} mode is totally forbidden in this frequency range with L_1/L =0. As L_1/L goes up gradually, it gives rise to the reduction of the bandwidth for single high order mode operation thanks to the decrease of the bandgap in Fig. 2(b). When the ridges are arranged with glide symmetry L_1/L=1/2, the amplitudes of TE_{10}^{2w} and TE_{20}^{2w} modes are nearly the same. It suggests that the single high order operation is no longer permitted in this case.

III. RESULTS AND DISCUSSION

To experimentally characterize the phenomenon of single high-order mode operation, we design and fabricate a prototype of the waveguide that only supports TE_{20}^{2w} mode, as shown in Fig. 4(a). There are two rows and thirteen columns of ridges inside the sample. As the launcher

of the TE_{20}^{2w} mode, a narrow waveguide that only operates with TE_{10}^{w} mode is connected on the right for mode conversion as mentioned in Fig. 3. The dimensions of the waveguide and these periodic ridges are identical to the design in Fig. 3(a). The only difference is that the ideal waveguide ports which are used to stimulate the desired waveguide modes, are replaced by coaxial probes for practical excitation. Because of the fact that TE_{20}^{2w} mode can be considered as the combination of two TE_{10}^{w} modes with reversed phase in the transverse cross sections as shown in Figs. 2(b) and (d), the ideal waveguide Port-2 in Fig. 3(a) can be replaced by two independent coaxial probes. Under the condition of TE_{20} mode, the signals of these two ports (port 2 and 3 in Fig. 4(a)) must be out of phase and of uniform amplitude.

The S-parameters of the three-port network are measured by the network analyzer Agilent N5230C. If Port-3 is connected by a matched load, we can measure the transmission coefficient S_{21} from Port-1 to Port-2. Similarly, we can get S_{31} in the same way. Fig. 4(b) and (c) show the simulated transmission coefficients ($|S_{21}|$ and $|S_{31}|$) and the phase difference ($\angle S_{21} - \angle S_{31}$) for different values of L_1/L. For an ideal TE_{20} mode, S_{21} and S_{31} should be out of phase. The gray region in Fig. 4(c) highlights the range with 180±5°. It can be found that the bandwidth with opposite phase starts from 9.9 to 12.1 GHz when L_1/L=0, and then narrows gradually as L_1/L goes up. The results are consistent with the theoretical prediction in Fig. 3, since the bandgap of TE_{10} mode reduces with the increase of L_1/L. The measured transmission amplitudes and phases with L_1/L=0 are presented in Fig. 4(d). Obviously, the numerical and experimental results (depicted in Fig. 4(b) and (c)) agree closely in the whole frequency range. The subtle discrepancy of the performance between Fig. 3 and Fig. 4 in various parts can be attributed to the impedance mismatch, since the coaxial feeding structures employed in Fig. 4 have a nearly constant impedance of 50 Ohm within the whole operation bandwidth.

The aforementioned method can be easily extended to generate a high order TE_{n0} mode (n> 2) for single mode operation, which offers a large degree of freedom for mode manipulation within the waveguide. To prove its feasibility, we simply broaden the waveguide width allowing three ridges aligned in the lateral direction as depicted in Fig. 5(a), therefore the

TE_{30}^{3w} mode can be supported in this case. As stated before, the TE_{30}^{3w} mode actually has identical dispersion properties with TE_{10}^{w} and TE_{20}^{2w} modes in Fig. 5(a). Here, we plot the dispersion curves of the first three modes (TE_{10}^{3w}, TE_{20}^{3w} and TE_{30}^{3w} modes) with L_1/L=0 in Fig. 5(b). It is clear that in the bandgap of the TE_{10}^{3w} mode, there exist two modes, namely, TE_{20}^{3w} and TE_{30}^{3w} modes that can propagate freely. Moreover, in the gray region of Fig. 5(b), only TE_{30}^{3w} mode can be supported in that frequency range as predicted in the previous theoretical analysis.

To further suppress the TE_{20}^{3w} mode and expand the single mode operation bandwidth, the feeding position should be carefully taken into account. Due to the odd symmetry of the TE_{20} mode at the transverse cross section [see Fig. 2(d)], the modal electric field is supposed to be zero at the center. Therefore, if the waveguide is fed by coaxial probes at this point, the TE_{20} mode can hardly be excited due to the field mismatch. This can be verified by considering the central feeding and side feeding respectively in Fig. 5(c). From the simulated mode conversion rates depicted in Fig. 5(e), it can be found that the TE_{20}^{3w} mode is significantly suppressed with the central feeding, and the single mode operation bandwidth for TE_{30}^{3w} mode is nearly doubled compared to the side feeding case. Fig. 5(d) shows the electric field distribution of *z* component in the *xoy* plane.

Fig. 6(a) shows the fabricated sample to verify the capability of bandgap adjustment with reduced glide symmetry. Consistent with the fabricated example in Fig. 4, here L_1/L is selected to be 0.25. Fig. 6(b) gives the simulated dispersion diagrams of the designed TE_{30}^{3w} mode waveguide. The simulated transmission amplitudes and phase differences ($\angle S_{21} - \angle S_{31}$, $\angle S_{21} - \angle S_{41}$) are given in Fig .6(c). It can be seen, the curves of amplitudes (S_{31} and S_{41}), phase

differences ($\angle S_{21} - \angle S_{31}$ and $\angle S_{21} - \angle S_{41}$) are overlapped, which is attributed to the suppression of TE_{30}^{2w} mode, as shown in Fig. 5(e). The measured results are given in Fig. 6(d). The antiphase range (180±5°) covers from 9.9 to 11.7 GHz, which is consistent with the gray region in Fig. 6(b).

IV. CONCLUSIONS

We proposed high-order guiding mode generations with the protection of reduced symmetry. A TE_{20} mode generator was designed in the X band, by loading periodic metallic ridges with reduced glide symmetry in the waveguide. The physical dimension of the unit cell is optimized to enable an overlap of the low order mode bandgap and a high order mode spectrum, which corresponds to the working band of TE_{20} mode. Different from the traditional high order mode generator, the proposed method can be capable of modifying the working range independently by reducing the symmetry of the guiding structure. To demonstrate the ability of high order modes generation with n>2, one TE_{30} mode generator is achieved by the synergy of the low order mode bandgaps and feeding network with the symmetry of TE_{30} mode in the transverse section which guarantee the unicity of TE_{30} mode in the working band. The simulated and measured results indicate the unicity of TE_{n0} mode and the tunability of bandwidth which is applicable in various areas where modes elimination or generation are required.

ACKNOWLEDGEMENTS

This work was supported in part from the National Key Research and Development Program of China (2018YFA0701904, 2017YFA0700201, 2017YFA0700202, and 2017YFA0700203), the National Science Foundation of China (61731010 and 61722106), and the 111 Project (111-2-05).

REFERENCES

[1] D. M. Pozar, *Microwave Engineering* (John Wiley & Sons, New York, 2009).

[2] S. Deng, D. Pommerenke, T. Hubing, and D. Shin, An experimental investigation of high order mode suppression in TEM cells, IEEE Trans. Electromagn. Compat. 50, 416 (2008).

[3] I. Arregui, F. Teberio, I. Arnedo, A. Lujambio, M. Chudzik, D. Benito, T. Lopetegi, R. Jost, F. Görtz, J. Gil, et al., High-power low-pass harmonic filters with higher-order TE_{n0} and non-TE_{n0} mode suppression: design method and multipactor characterization, IEEE Trans. Microw. Theory Tech. 61, 4376 (2013).

[4] Z. Zhang, J. Luo, and Z. Zhang, Analysis and suppression of high-order mode oscillation in an S-band klystron, IEEE Trans. Plasma Sci. 43, 515 (2015).

[5] F. Teberio, I. Arregui, A. Gomez-Torrent, E. Menargues, I. Arnedo, M. Chudzik, M. Zedler, F. Görtz, R. Jost, T. Lopetegi and M. A. G. Laso, High-power waveguide low-pass filter with all-higher-order mode suppression over a wide-band for Ka-band satellite applications, IEEE Microw. Wirel. Co. 25, 511 (2015).

[6] D. Jia, Q. Feng, Q. Xiang, and K. Wu, Multilayer substrate integrated waveguide (SIW) filters with higher-order mode suppression, IEEE Microw. Wirel. Co. 26, 1 (2016).

[7] S. G. Tantawi, C. D. Nantista, V. A. Dolgashev, C. Pearson, J. Nelson, K. Jobe, J. Chan, K. Fant and J. Frisch, High-power multimode X-band rf pulse compression system for future linear colliders, Phys. Rev. Spec. Top. -Accel. Beams. 8, 527 (2005).

[8] C. D. Nantista and S. G. Tantawi, Multi-moded passive rf pulse compression development at SLAC, in AIP Conference Proceedings 569, 702 (2001).

[9] S. G. Tantawi, C. D. Nantista, G. B. Bowden, K. S. Fant, N. M. Kroll, and A. E. Vlieks, Evaluation of the TE_{12} mode in circular waveguide for low-loss, high-power rf transmission, Phys. Rev. ST Accel. Beams 5, 082001 (2002).

[10] V. L. Granatstein and W. Lawson, Gyro-amplifiers as candidate RF drivers for TeV linear colliders, IEEE Trans. Plasma Sci. 24, 648 (1996).

[11] I. Spassovsky, E. S. Gouveia, S. G. Tantawi, B. P. Hogan, W. Lawson, and V. L. Granatstein, Design and cold testing of a compact TE_{10}–TE_{20} mode converter, IEEE Trans. Plasma Sci. 30, 787 (2002).

[12] G. R. P. Marie, Mode transforming mode transition, U.S. Patent 2859412 (1958).

[13] W. A. Huting and K. J. Webb, Comparison of mode-matching and differential equation techniques in the analysis of a waveguide transitions, IEEE Trans. Microw. Theory Tech. 39, 280 (1991).

[14] M. Yeddulla, S. Tantawi, J. Guo, and V. Dolgashev, An analytical design and analysis method for a high-power circular to rectangular waveguide mode converter and its applications, IEEE Trans. Microw. Theory Tech. 57, 1516 (2009).

[15] M. Belaid, R. Martinez, and K. Wu, A mode transformer using fin-line array for spatial power-combiner applications, IEEE Trans. Microw. Theory Tech. 52, 1191 (2004).

[16] J. Xu, N. C. Zhi, X. Qing, and H. Wei, A single-layer SIW slot array antenna with TE20 mode, Asia-Pac. Microwave Conf. Proc. (2011).

[17] W. Peng, J. Liu, and X. Quan, Wideband excitation technology of mode substrate integrated waveguide (SIW) and its applications, IEEE Trans. Microw. Theory Tech. 63, 1863 (2015).

[18] J. Xu, Z. N. Chen, X. Qing, and W. Hong, 140-GHz-mode dielectric-loaded SIW slot antenna array in LTCC, IEEE Trans. Antennas Propag. 61, 1784 (2013).

[19] J. Bae, M. Fujita, and K. Mizuno, A W-band overmoded-waveguide oscillator with Gunn diodes, IEEE Trans. Microw. Theory Tech. 49, 2554 (2000).

[20] S. Matsumoto, I. Ohta, K. Fukada, T. Kawai, K. Iio, and T. Kashiwa, A TE10-TE20 mode transducer utilizing a right-angled corner and its application to a compact H-plane out-of-phase power divider, Asia-Pac. Microwave Conf. Proc. (2009).

[21] H. Ikeuchi, T. Kawai, M. Kishihara, and I. Ohta, Design of TE10-TE30 mode transducer using H-plane waveguide corner, Asia-Pac. Microwave Conf. Proc. (2012).

[22] H. Ikeuchi, S. Matsumoto, T. Kawai, and I. Ohta, A novel TE10–TE20 mode transducer utilizing vertical cross-excitation, IEEE MTT-S Int. Microwave Symp. (2010).

[23] A. A. Kirilenko, L. A. Rud, and V. I. Tkachenko, Nonsymmetrical H-Plane Corners for TE10–TEq0 Mode Conversion in Rectangular Waveguides, IEEE Trans. Microw. Theory Tech. 54, 2471 (2006).

[24] A. J. Martinez-Ros, M. Bozzi, and M. Pasian, Double-sided SIW leaky-wave antenna with increased directivity in the E-plane, IEEE Trans. Antennas Propag. vol. 66, 3130 (2018).

[25] P. J. Crepeau and P. R. Mcisaac, Consequences of symmetry in periodic structures, Proc. IEEE. 52, 33 (1963).

[26] L. Brillouin, *Wave Propogation in Periodic Structures: Electric Filters and Crystal Lattices* (McGraw-Hill, 1946).

[27] D. A. Watkings, *Topics in Electromagnetic Theory* (John Wiley & Sons, 1958)

[28] R. E. Collin, *Foundations for Microwave Engineering* (McGraw-Hill, 1966)

[29] J. R. Pierce, Coupling of Modes of Propagation, J. Appl. Phys. 25, 179 (1954).

[30] A. Hessel, H. C. Ming, R. C. M. Li, and A. A. Oliner, Propagation in periodically loaded waveguides with higher symmetries, Proc. IEEE. 61, 183 (1973).

[31] A. Hessel and A. Oliner, *Electromagnetic Wave Theory* (Elsevier, 1967).

[32] W. Wang, Z. Zheng, X. Fang, H. Zhang, M. Jin, J. Lu, Q. Luo and S. Gao, A waveguide slot filtering antenna with an embedded metamaterial structure, IEEE Trans. Antennas Propag. 67, 2953 (2019).

[33] Q. Huang, W. Wang, W. Jin, and K. Chiang. Ultra-broadband mode filter based on phase-shifted long-period grating, IEEE Photonics Technol. Lett. 21, 1052 (2019).

Figure Captions

Fig. 1 (a-b) Schematic of an empty rectangular waveguide and the corresponding dispersion diagram. (c-e) Schematic of a rectangular waveguide with periodic loading, and the corresponding dispersion diagrams before and after parameter adjustment.

Fig. 2 (a-b) Structural views of the periodically loaded waveguides with one and two metallic ridges in the lateral direction (h=10 mm, h_r=2 mm, L=14 mm, W=18 mm, a=13 mm, b=3 mm and L_1=0 ~ 7 mm) and the electric field distributions in *xoz* cross section. (c) Electric field distributions of TE_{10}, TE_{20} and TE_{30} modes with the waveguide width of w, $2w$ and $3w$ respectively. (d) Dispersion curves of the periodically loaded waveguide with two metallic ridges in the transverse direction.

Fig. 3 (a) Top and side views of the TE_{20} mode generator, where the dotted rectangles indicate the taper regions with gradually changed ridges to improve impedance matching. (b) Distribution of the electric field E_z in the *xoy* plane. (c) Simulated transmission coefficients S_{21} from TE_{10}^{w} to TE_{10}^{2w} modes, and TE_{10}^{w} to TE_{20}^{2w} modes, when L_1/L varies from 0 to 0.5.

Fig. 4 (a) Photograph of the fabricated TE_{20} mode generator, which is excited by a coaxial probe. (b) Simulated transmission coefficients S_{21} and S_{31} when L_1/L is 0, 0.25, and 0.43 respectively. (c) Simulated phase differences between Port 2 and Port 3 when L_1/L is 0, 0.25, and 0.43 respectively. (d) Measured transmission coefficients and phase difference when L_1/L is 0.25.

Fig. 5 (a) TE_{30} waveguide and the corresponding electric field distribution in the *xoz* plane. (b) Dispersion curves of TE_{10}^{3w}, TE_{20}^{3w} and TE_{30}^{3w} modes with L_1/L=0. (c) TE_{30}^{3w} mode generation with side and central feeding. (d) Distribution of the simulated electric field E_z in the *xoy* plane with central feeding. (e) Simulated transmission coefficients S_{21} from TE_{10}^{w} to TE_{10}^{3w} modes, TE_{10}^{w} to TE_{20}^{3w} modes and TE_{10}^{w} to TE_{30}^{3w} modes with L_1/L=0.

Fig. 6 (a) Photographs of the fabricated TE_{30} mode generator with L_1/L = 0.25. (b) Dispersion curves of TE_{10}^{3w}, TE_{20}^{3w} and TE_{30}^{3w} modes with L_1/L=0.25. (c) Simulated amplitudes of S-parameters and the phase differences (Port2-Port3). (d) Measured S_{21} and S_{31}, and the corresponding phase difference between Port 2 and Port 3.

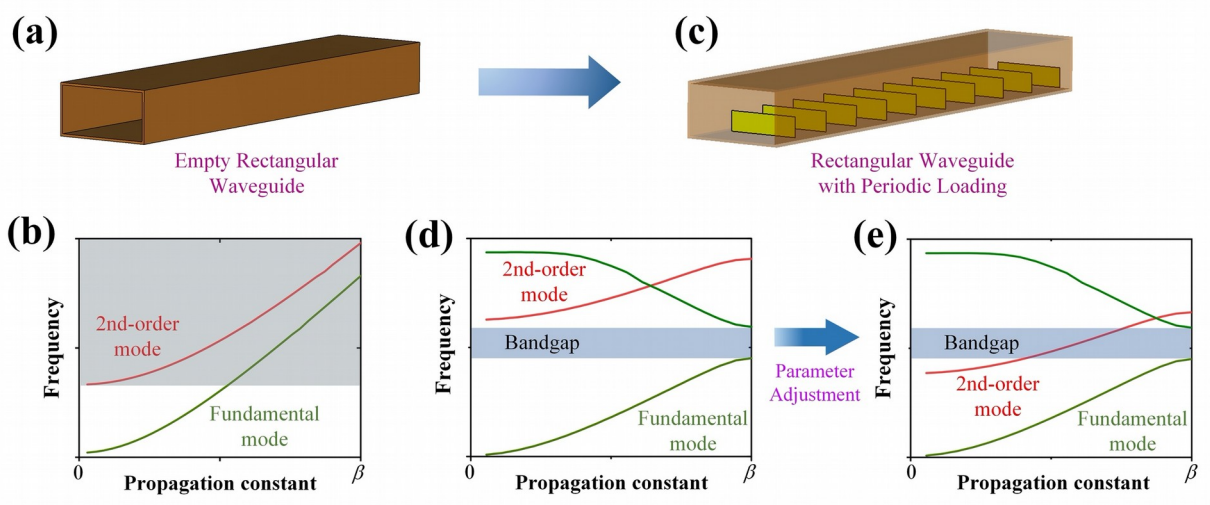
(a)
Empty Rectangular Waveguide
(c)
Rectangular Waveguide with Periodic Loading
(b)
Frequency
2nd-order mode
Fundamental mode
0
Propagation constant
β
(d)
Frequency
2nd-order mode
Bandgap
Fundamental mode
0
Propagation constant
β
Parameter Adjustment
(e)
Frequency
Bandgap
2nd-order mode
Fundamental mode
0
Propagation constant
β

Fig. 1

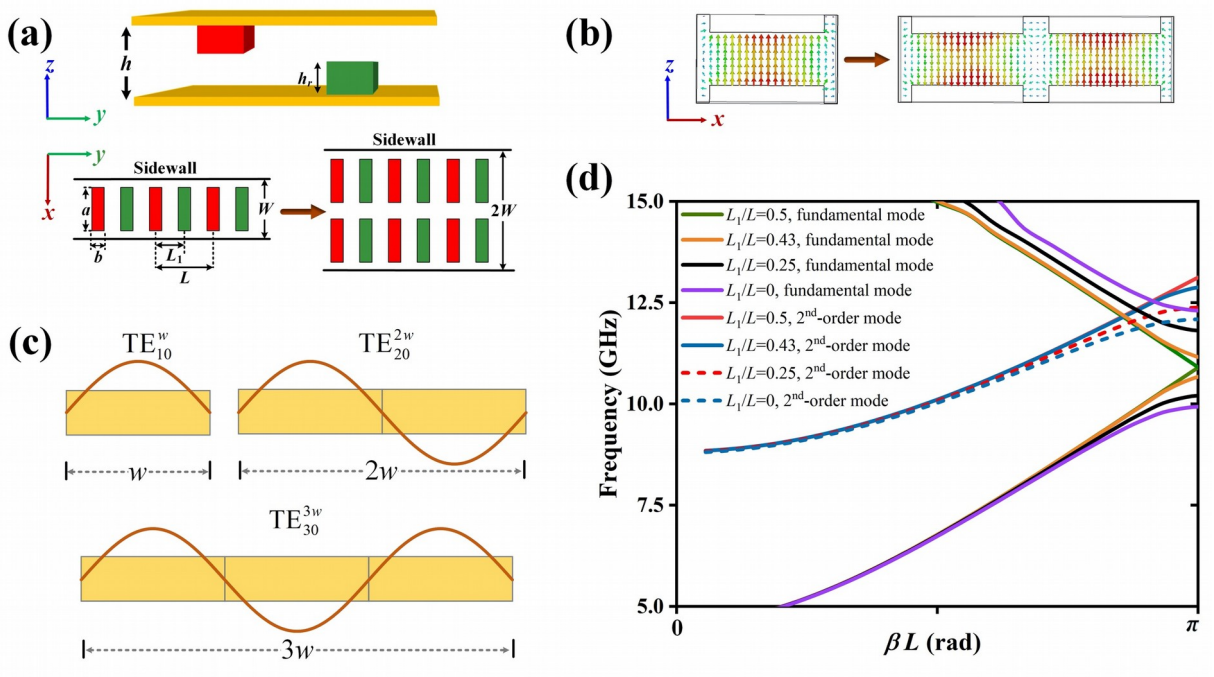
(a)
h
h_r
z
y
Sidewall
Sidewall
y
x
a
b
L_1
L
W
2W
(b)
z
x
(c)
TE_{10}^{w}
TE_{20}^{2w}
w
2w
TE_{30}^{3w}
3w
(d)
15.0
12.5
10.0
7.5
5.0
0
π
Frequency (GHz)
βL (rad)
L_1/L=0.5, fundamental mode
L_1/L=0.43, fundamental mode
L_1/L=0.25, fundamental mode
L_1/L=0, fundamental mode
L_1/L=0.5, 2nd-order mode
L_1/L=0.43, 2nd-order mode
L_1/L=0.25, 2nd-order mode
L_1/L=0, 2nd-order mode

Fig. 2

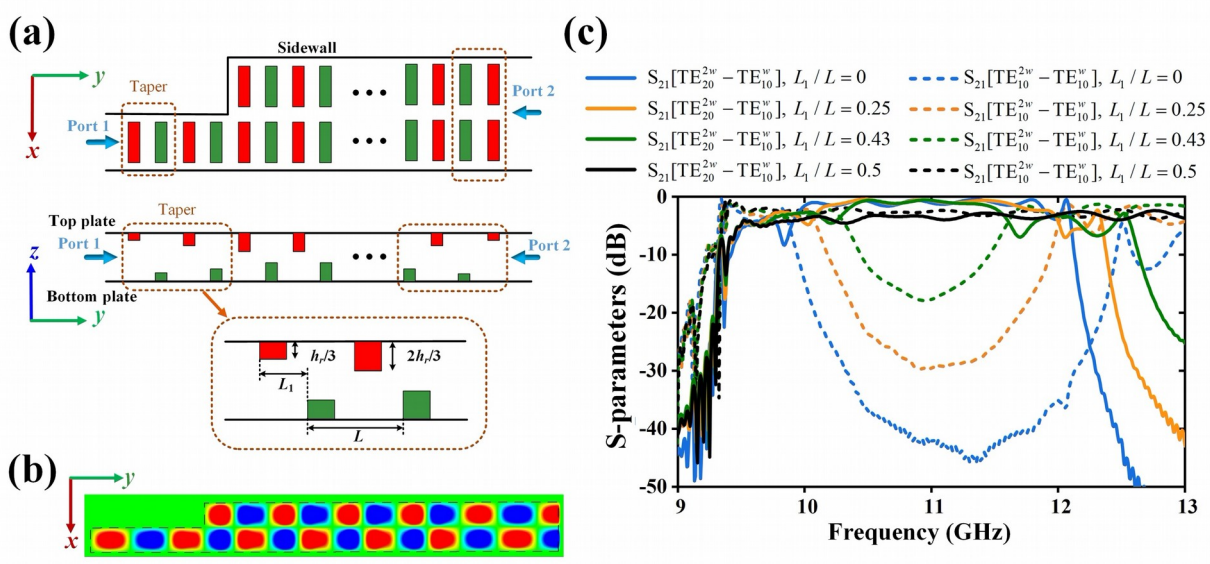
(a)
Sidewall
Taper
Port 1
Port 2
Top plate
Bottom plate
$h_r/3$
$2h_r/3$
L_1
L
(b)
(c)
$S_{21}[TE_{20}^{2w} - TE_{10}^{w}]$, $L_1/L = 0$
$S_{21}[TE_{10}^{2w} - TE_{10}^{w}]$, $L_1/L = 0$
$S_{21}[TE_{20}^{2w} - TE_{10}^{w}]$, $L_1/L = 0.25$
$S_{21}[TE_{10}^{2w} - TE_{10}^{w}]$, $L_1/L = 0.25$
$S_{21}[TE_{20}^{2w} - TE_{10}^{w}]$, $L_1/L = 0.43$
$S_{21}[TE_{10}^{2w} - TE_{10}^{w}]$, $L_1/L = 0.43$
$S_{21}[TE_{20}^{2w} - TE_{10}^{w}]$, $L_1/L = 0.5$
$S_{21}[TE_{10}^{2w} - TE_{10}^{w}]$, $L_1/L = 0.5$
S-parameters (dB)
Frequency (GHz)

Fig. 3

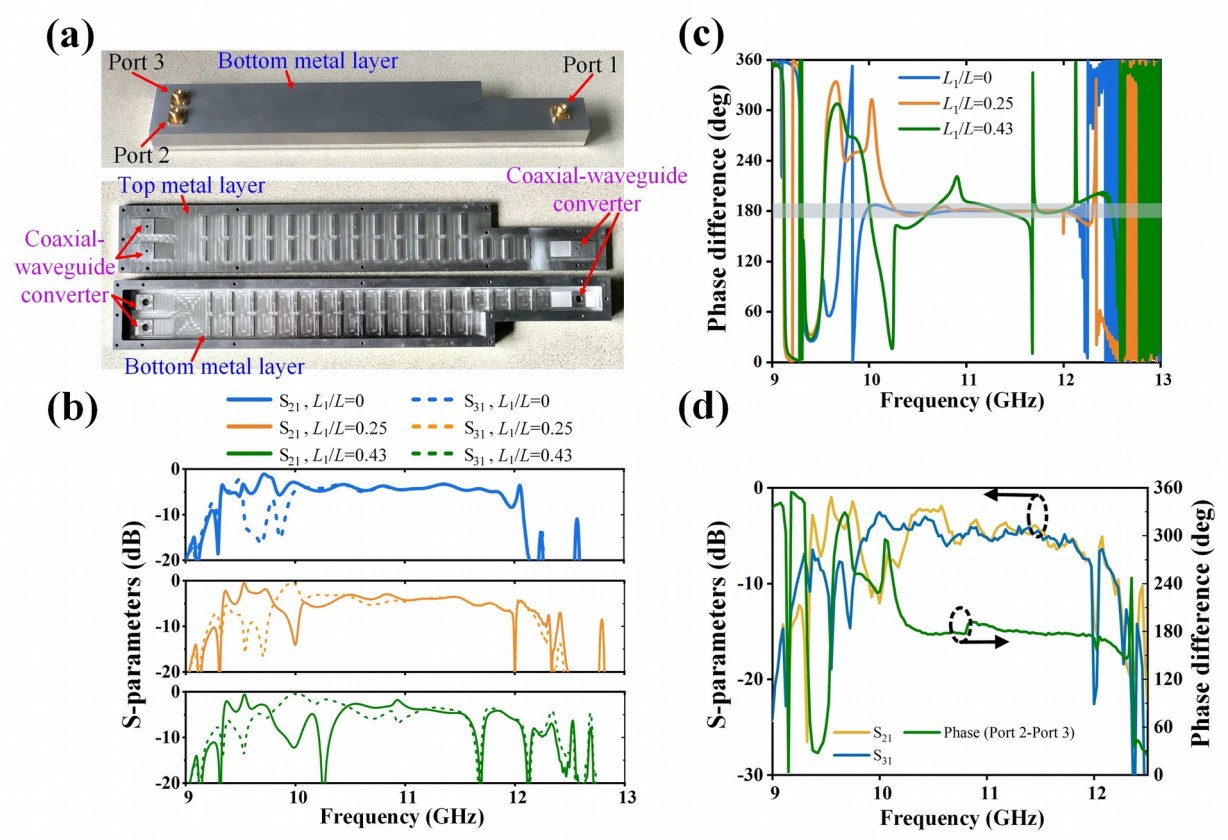
(a)
Port 3
Bottom metal layer
Port 1
Port 2
Top metal layer
Coaxial-waveguide converter
Coaxial-waveguide converter
Bottom metal layer
(b)
S21 , L1/L=0
S31 , L1/L=0
S21 , L1/L=0.25
S31 , L1/L=0.25
S21 , L1/L=0.43
S31 , L1/L=0.43
S-parameters (dB)
Frequency (GHz)
(c)
L1/L=0
L1/L=0.25
L1/L=0.43
Phase difference (deg)
Frequency (GHz)
(d)
S-parameters (dB)
Phase difference (deg)
S21
S31
Phase (Port 2-Port 3)
Frequency (GHz)

Fig. 4

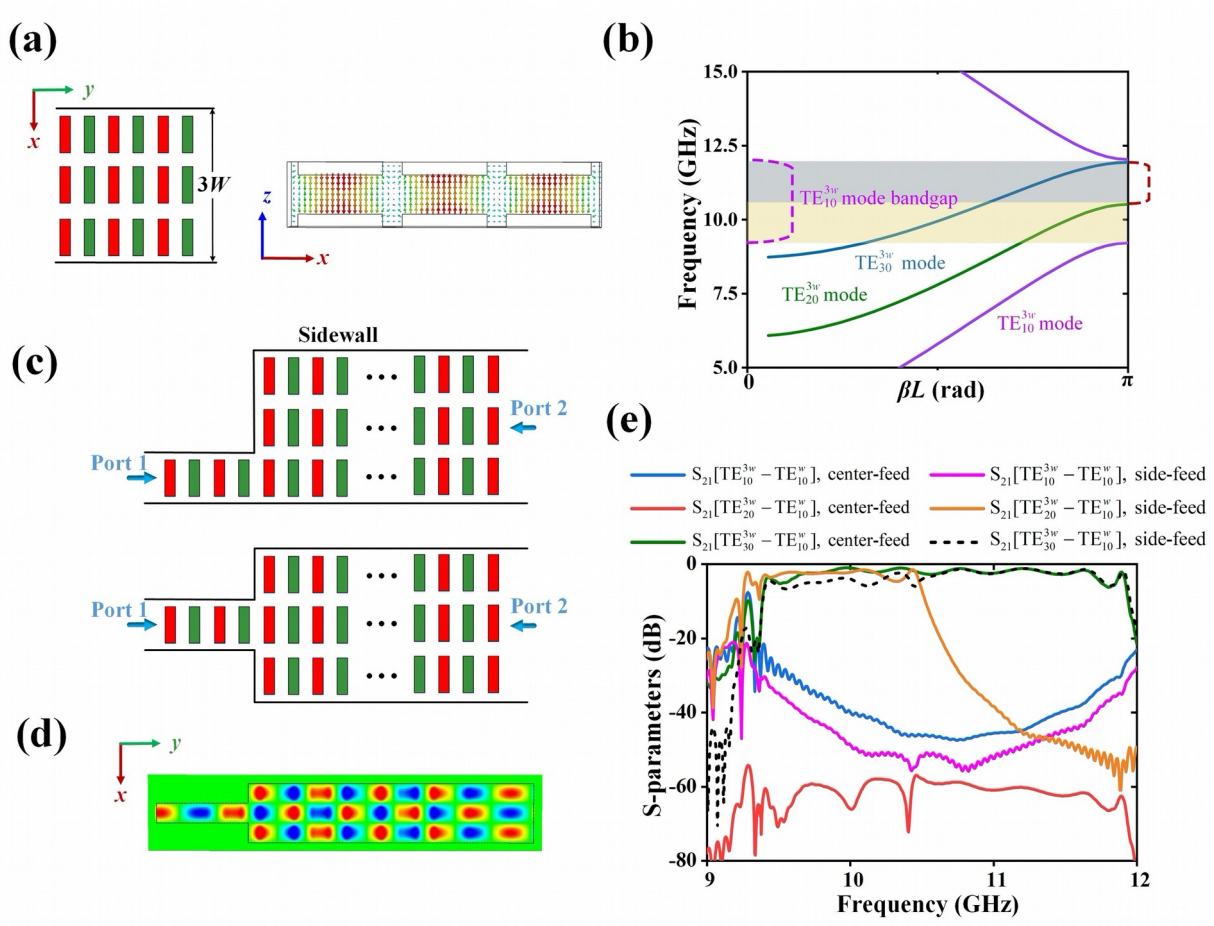
(a)
y
x
3W
z
x
(b)
15.0
12.5
10.0
7.5
5.0
Frequency (GHz)
TE10 3w mode bandgap
TE30 3w mode
TE20 3w mode
TE10 3w mode
0
βL (rad)
π
(c)
Sidewall
Port 2
Port 1
Port 1
Port 2
(d)
y
x
(e)
S21[TE10 3w − TE10 w], center-feed
S21[TE10 3w − TE10 w], side-feed
S21[TE20 3w − TE10 w], center-feed
S21[TE20 3w − TE10 w], side-feed
S21[TE30 3w − TE10 w], center-feed
S21[TE30 3w − TE10 w], side-feed
0
-20
-40
-60
-80
S-parameters (dB)
9
10
11
12
Frequency (GHz)

Fig. 5

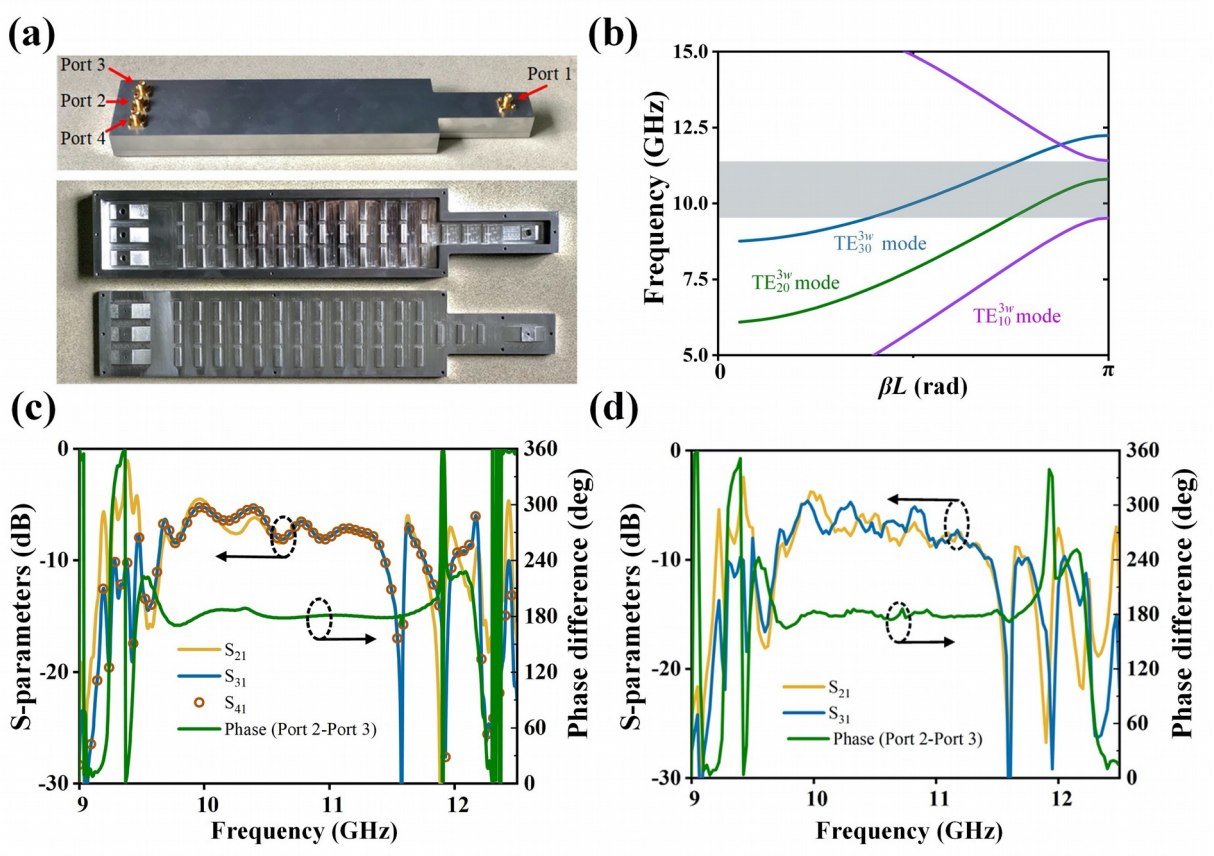
(a)
Port 3
Port 2
Port 4
Port 1
(b)
Frequency (GHz)
15.0
12.5
10.0
7.5
5.0
0
π
βL (rad)
TE30 3w mode
TE20 3w mode
TE10 3w mode
(c)
S-parameters (dB)
Phase difference (deg)
Frequency (GHz)
S21
S31
S41
Phase (Port 2-Port 3)
(d)
S-parameters (dB)
Phase difference (deg)
Frequency (GHz)
S21
S31
Phase (Port 2-Port 3)

Fig. 6